Journal of Manufacturing Processes 80 (2022) 458–468

Contents lists available at ScienceDirect

Journal of Manufacturing Processes

journal homepage: www.elsevier.com/locate/manpro

Robustness evaluation of control algorithms for a long-stroke fast tool servo

Zheng Gong [a], Dehong Huo [a,*], Zengyuan Niu [b], Wanqun Chen [c], Kai Cheng [d]

[a] School of Engineering, Newcastle University, Newcastle upon Tyne NE1 7RU, UK
[b] Uptech, Jiangsu Industrial Technology Research Institute, Kunshan, Jiangsu Province 215300, China
[c] School of Electromechanical Engineering, Soochow University, Soochow 215031, China
[d] School of Engineering and Design, Brunel University, London UB8 3PH, UK

ARTICLE INFO

Keywords:
Fast tool servo
Control algorithm
Tracking error
Robustness
Microstructured surface

ABSTRACT

Fast tool servo (FTS) is an effective freeform surface machining technology in precision machining. The robustness of the FTS control algorithm is an important factor influencing the quality of machining. In this paper, an advanced PID control algorithm and a hybrid control algorithm are tested on a Lorentz force FTS. A mathematical simulation model is built according to the system characteristics. The model is verified by the system identification model and used for the simulation of the system's motion under disturbance. Simulation results show that the advanced PID control results in more significant differences in tracking error, amplitude error, and phase errors than the hybrid control. Four machining experiments are designed and conducted. The motion profile results from simulations and experiments show that the hybrid control (<0.5% tracking error) has better robustness than advanced PID control (>1.5% tracking error). In addition, the hybrid control exhibits rapid response speed. From the 3D profile of the machined microstructured surface, the hybrid control helps to achieve better form accuracy in the workpiece than the advanced PID control.

1. Introduction

Fast tool servo (FTS) is one of the key technologies in the precision machining of freeform surfaces. FTS is realized by a separate control system and is usually installed on an ultra-precision turning machine. The FTS control system can generate a reciprocating motion on the cutting tool. The tool path is generated by combining the motion at the machine axes and that of the FTS according to the surface profile requirements [1,2]. The moving mass of the FTS is small, which leads to high working frequency and hence high machining efficiency. Good surface quality is another main advantage of using FTS technology.

Two main types of FTS have been widely developed in recent years: piezoelectric FTS (PZT-FTS) and Lorentz force (LF-FTS). PZT-FTS employs piezoelectric ceramics as the actuator and flexure hinges as the guide system. A short stroke and high working frequency are its main characteristics. Sosnicki et al. [3] developed the servo piezo tool SPT400 MML in which a 400 μm stroke with a working bandwidth of above 450 Hz was achieved. Zhu et al. [4] conducted a multi-objective optimum design study, and the final system achieved a 10.25 μm stroke and working bandwidth at a minimum of 2 kHz. Wang et al. [5] used a motion amplifier to reach a 300 μm stroke, and a 321 Hz sinusoidal signal was tested on the designed PZT-FTS. Meanwhile, LF-FTS adopts a linear motor as the driving source, with an air bearing or flexure hinge as the guide system. This type of FTS system has a long stroke but low working frequency. Tian et al. [6] designed an LF-FTS system with a voice coil motor and a T-shaped slide. A sinusoidal signal test with a 5 mm stroke at 50 Hz was conducted on the designed system. A similar LF-FTS used to fabricate freeform progressive addition lenses was presented by Feng et al. [7]. This system has an 8 mm stroke and the recorded response in tracking a sinusoidal motion was a 3 mm stroke at 16.67 Hz. Liu et al. [8] have also introduced a new long-stroke LF-FTS for the machining of non-rotational symmetrical optics. The system was built using a linear motor, an air bearing, a high-resolution encoder and a motion controller.

Apart from the mechanical design, the design of the control system is another important aspect of the FTS system. Numerous FTS control algorithms have been reported in the literature, and these are summarised in this section. Proportion-integration-differentiation (PID) control is widely used in the early stage of control algorithm development. Rakuff et al. [9] used a PID controller with linear and nonlinear feedforward controllers to reduce the final tracking error to <0.2% with a 500 μm stroke under a 10 Hz input sinusoidal command signal. Repetitive

* Corresponding author.
E-mail address: dehong.huo@newcastle.ac.uk (D. Huo).

https://doi.org/10.1016/j.jmapro.2022.06.017
Received 4 March 2022; Received in revised form 9 May 2022; Accepted 8 June 2022
Available online 19 June 2022

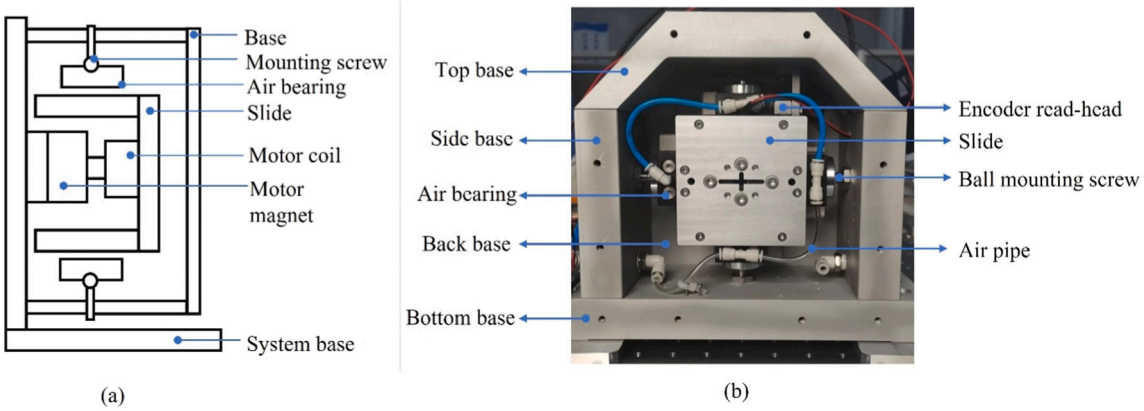

Fig. 1. Designed FTS system: (a) schematic design; (b) front view.

control is another widely used type of control algorithm for FTS systems, and it is suitable for the control of periodic signals. Lu et al. [10,11] designed a repetitive control algorithm with two resonators for an FTS system, where the tracking error is decreased from 1.048 μm to 0.0148 μm. PID control and repetitive control can be integrated for a PZT-FTS, as demonstrated by Zhou et al. [12] where the final tracking error is decreased to 8.5% of the original error.

Sliding mode control (SMC) is a control method with variable structure that does not rely on the mathematical control model of the system. This characteristic means that the SMC algorithm is suitable for PZT-FTS. Zhang et al. [13] combined a variable-rate approaching law and an exponential approaching law to design an SMC controller. The system tracking error is reduced from ±2.27% to ±0.57%. SMC and feedforward repetitive control were combined and developed for a PZT-FTS as demonstrated by Duan et al. [14], where the tracking error was reduced from 10.92% with the plain PID control to 0.82% under the proposed combined control algorithm. Meanwhile, active disturbance rejection control (ADRC) is an advanced control algorithm based on the PID control algorithm. Wu et al. [15] presented a novel ADRC algorithm that integrated a nonlinear PD controller and feedforward error compensation for an LF-FTS system. The cutting experiments showed a maximum tracking error of 4–5 μm when the cutting depth was varied from 0.1 mm to 0.4 mm. Zero phase error tracking control (ZPETC) is an effective solution for the phase delay problem, although this algorithm cannot be used independently and can be only used with other algorithms. Lin et al. [16] used the ZPETC in the form of a double-feedforward compensator with an inverse Prandtl–Ishlinskii model for a PZT-FTS. For LF-FTS, ZPETC can be designed as a velocity/acceleration feedforward control according to the desired motion. A ZPETC was integrated into a PID controller and applied on an LF-FTS [17]. Some machine learning algorithms like neural network control [18] and fuzzy control [19] have also been explored to further develop FTS control systems and to render the system capable of allowing online tuning ability.

Most current research is focused on solving the hysteresis problem in PZT-FTS, and little research has been conducted on the LF-FTS control algorithm in order to tackle the challenge of its undamped characteristics due to the use of voice coil motors and air bearings. As a machining technology, the FTS system will experience cutting force and other disturbances. The system response under external disturbance is a key factor influencing the quality of machining. Therefore, the robustness of different control algorithms is another issue which requires investigation. Existing research focuses on improving system performance at the no-load condition, but the robustness of the control system during actual machining is more important.

In this paper, a long-stroke LF-FTS system is designed which consists of a voice coil motor, a square slide and four air bearings. A mathematical model is built and tested by a system identification model. Two different control algorithms, namely advanced PID control and hybrid control, are designed based on previous work [20]. The robustness of these two algorithms is tested through system simulations and actual machining experiments.

2. Mechanical subsystem design

As shown in Fig. 1, the motor magnet is fixed to the system's back base, and the motor coil is connected to a hollow square slide through a connection plate. Four designed air bearings are located around the slide and are connected to the system base through ball-headed mounting screws. The air bearings can lift the slide and reduce friction to a negligible level, and the ball-headed screw offers self-levelling ability to the air bearing. The mechanical subsystem enables the reciprocating motion of the slide and the motor coil.

Motor selection is important for system performance. The system's reciprocating motion can be described as a sinusoidal motion, and the relationship between amplitude, frequency and motor force can be described as in Eqs. (1) and (2).

$$X = A \bullet sin(2\pi ft) \tag{1}$$

$$F = m \bullet a = m \bullet \ddot{X} = -m \bullet (2\pi ft)^2 \bullet A \bullet sin(2\pi ft) \tag{2}$$

where:X is the system motion profile (m); a is acceleration (m/s^2); t is time (s); A is the maximum amplitude (m); f is the working frequency (Hz); F is the driving force (N); and m is the mass of all of the moving components (Kg).

The maximum stroke and working frequency are designed as ±1.5 mm and 100 Hz. A linear voice coil motor with 64.6 N continuous force (*Moticont*, LVCM-070-038-01) is chosen. The air bearing is designed as a seven-orifice air bearing with a stiffness of 31.05 N/μm. The slide and system bases are made from aluminium to minimise mass. The moving mass of the system is 995.1 g.

3. Control algorithm robustness simulation

3.1. Control subsystem design

The control subsystem includes a multi-axis precision motion controller (*Omron* CK3M) and a motor drive (*Elmo* Gold Hornet). The DSP (Digital Signal Process) controller CK3M was chosen because it allows user-defined control algorithms to be implemented. A high resolution optical linear encoder (*Renishaw, Ti2000*) is used as a feedback element to form the positional closed loop. The system also includes a current loop in the motor drive. The controller generates the desired signal in the form of analogue signals (±10 V), which are transferred to the motor drive. The motor drive functions as the current loop, and it can

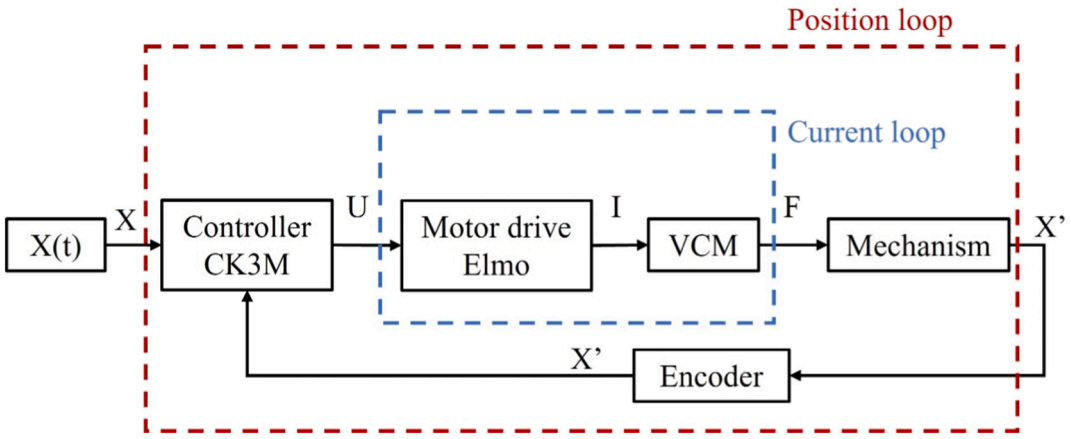

Fig. 2. Control block diagram of the FTS system.

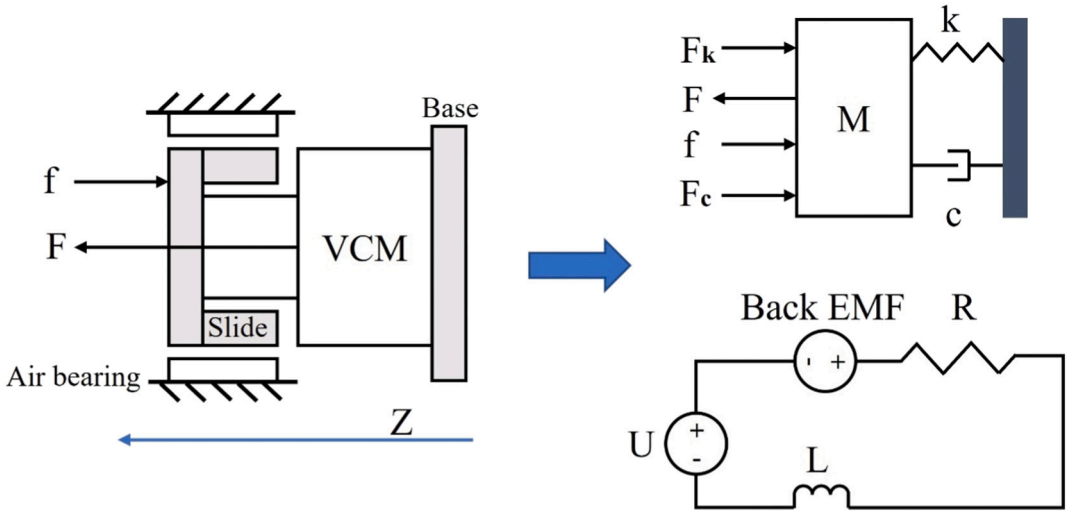

Fig. 3. Mechanical model and circuit model of the FTS system.

enlarge the current at a specific scale and maintain the current signal in a stable state to prevent current overshoot. The motor drive output signal is then transferred to the voice coil motor. The linear encoder detects movement, and generates a position signal which is sent back to the controller. The encoder generates a digital signal with 1 motor unit (mu) corresponding to 10 nm (1 mu = 10 nm). Therefore, the feedback can be considered to be linear. For example, for a system with a servo frequency of 16 kHz and if the desired motion signal is ±1 mm at 30 Hz, the controller will generate a sine signal of 100,000 mu at 30 Hz. The controller will calculate this digital signal according to the position loop control algorithms and transform it into voltage signals. The motor drive amplifies the voltage signal and can be considered as a PI controller for the current loop. The block diagram of this control system is shown in Fig. 2.

To build the control simulation model for the system, a mathematical model of the system must first be built according to its mechanical and electrical characteristics. The system can be simplified as a single degree of freedom in the direction of motion. The mechanical and circuit models of the system are shown in Fig. 3, and the corresponding equations are shown in Eqs. (3)–(5).

$$U = L\frac{di}{dt} + Ri + k_b v \tag{3}$$

$$F - f + F_k + F_c = Ma \tag{4}$$

$$F = k_c i; F_k = kx; F_c = cv \tag{5}$$

where:U is the system voltage (V); L is the inductance (H); i is the current (A); R is the resistance (Ω); k_b is the back electromotive force (EMF) constant; F is the driving force (N); f is the cutting force (N); F_k is the elastic force (N); F_c is the viscous force (N); M is the moving mass (Kg); a is the acceleration (m/s^2); k_c is the force constant (N/A); k is the elastic constant (N/m); x is the system motion (m); c is the damping constant (N/(m/s)); and v is the velocity (m/s).

The system's transfer function can be calculated using Eq. (6), in which F_k and F_c have been omitted due to the negligible stiffness and damping of the air bearings. The system is a predictable undamped system, and system identification is conducted using the frequency sweep method so as to obtain an accurate system model.

$$G(s) = \frac{x(s)}{U(s)} = \frac{k_c}{MLs^3 + (MR)s^2 + kb^2} \tag{6}$$

3.2. System identification

System identification is used to test the accuracy of the system simulation model. An accurate simulation model can then be used to further develop the control algorithm and test the system's capacity to resist disturbance. In this study, the current loop is integrated into the FTS model. The motor driver adopts a PI controller in the current loop,

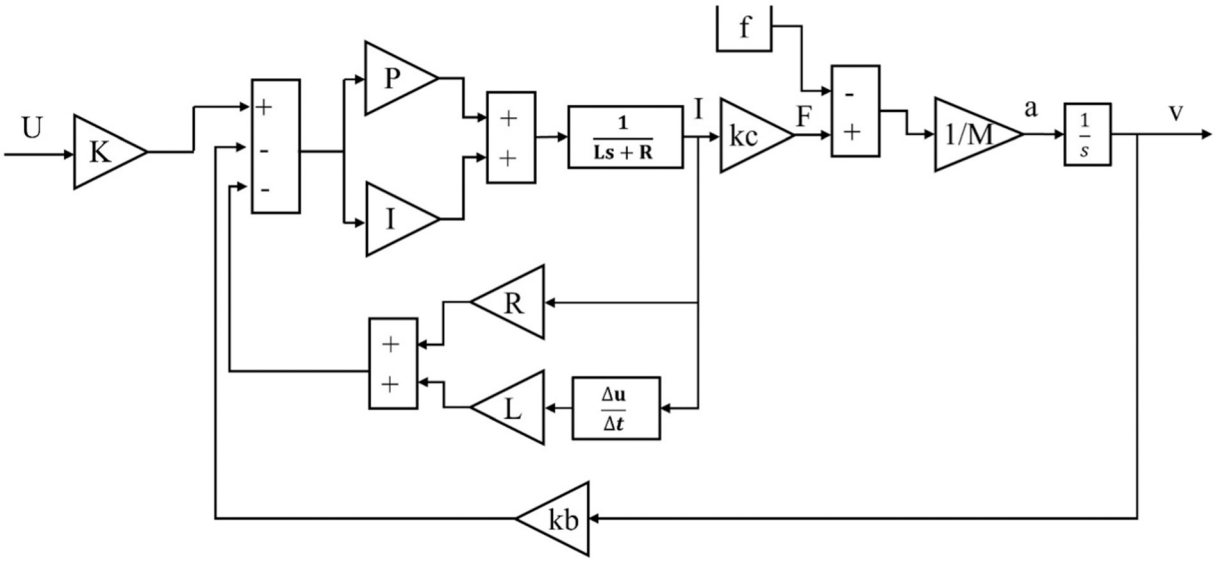

Fig. 4. Block diagram of the system simulation model.

Table 1
Model parameters.

Parameter	Symbol	Value	Parameter	Symbol	Value
Moving mass	M	1 Kg	Proportion	P	19.587
Motor force (Continuous)	F	64.6 N	Integration	I	1442.23
Cutting force (Maximum)	f	10 N	Resistance	R	4.3 Ω
Amplification constant	K	1.2	Inductance	L	2.4 mH
Input voltage	U	/	Force constant	kc	21.2 N/A
Output speed	v	/	Back EMF constant	kb	21.2 V/(M/S)

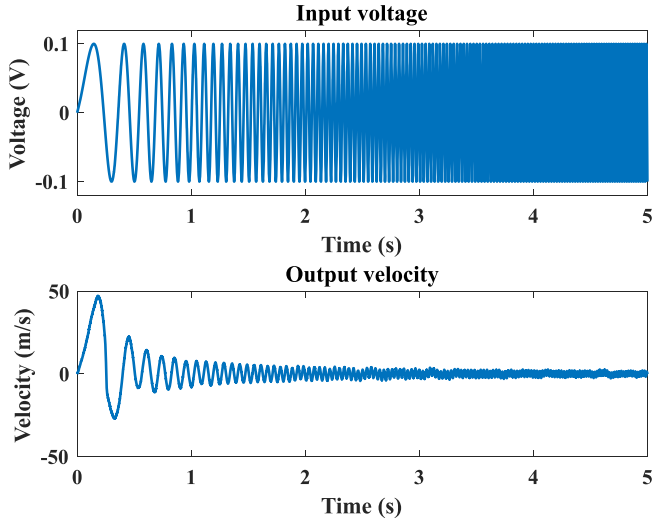

Fig. 5. Frequency sweep results.

and auto-tuning enables the current loop to have a bandwidth of 3 kHz while the current loop control parameters are fixed in the subsequent tests. Taking into account the system's transfer function and the current loop, the block diagram of the system simulation model is developed in Fig. 4. The model parameter descriptions are shown in Table 1.

The frequency sweep is realized by the controller. The frequency-varying voltage signal is transferred from the controller to the motor driver and drives the system to run at a certain speed. The velocity signal is calculated from the position signal through the encoder. The frequency sweep is an open-loop process that corresponds to the system simulation model. The frequency sweep results are shown in Fig. 5, and they can be used to calculate the state-space equations of the system as shown in Eq. (7).

$$\begin{cases} dx/dt = A\,x(t) + B\,u(t) + K\,e(t) \\ y(t) = C\,x(t) + D\,u(t) + e(t) \end{cases} \tag{7}$$

In the equation, $A = -10.7$, $B = -2.118$, $C = -2393$, $D = 0$, and $K = -5.94$.

The system identification model described in Eq. (7) is built using Simulink for comparison with the simulation model. A voltage signal with 1 V amplitude at 50 Hz is adopted as the input signal. The comparison process and results are shown in Fig. 6. In this comparison, the cutting force f is set to zero because the frequency sweep is carried out when the system has no extra load. From the comparison results, the simulation and identification results overlap after 0.28 s, and this overlapping trend continues until the end of the test. The simulation model shows some differences from the system identification model, especially during the initial periods. However, the simulation results show system velocity characteristics similar to the frequency sweep results. In the first three periods, the initial input voltage signal drives the system to move forward, and inertia force causes the system's nonlinear behaviour. Due to the open-loop design and the existence of the current loop, the change in sinusoidal voltage forces the system to exhibit a sinusoidal motion. The error in the range of overlapping is 2.87%. The comparison results show that the simulation model can reflect the motion characteristics of the actual system, and the simulation model can be used to test the robustness of the designed control algorithm for the position loop.

3.3. Robustness simulation model

Two different control algorithms, advanced PID and hybrid control, were implemented with the designed system, and the tracking performance under no-load conditions has been reported elsewhere [20]. Advanced PID is a standard servo control algorithm in the CK3M controller, and hybrid control is a novel control algorithm developed for the FTS system. The diagrams for the robustness test simulations and the

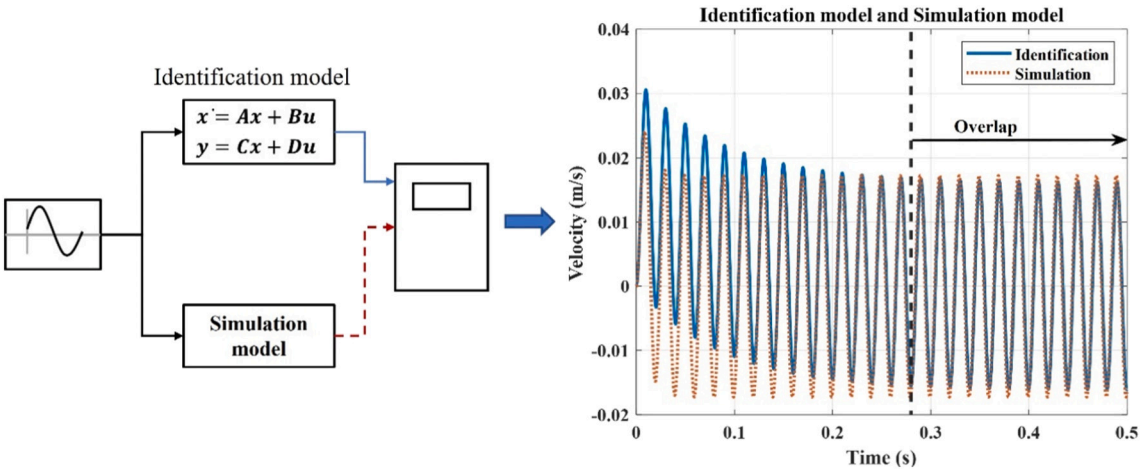

Fig. 6. Comparison of identification model and simulation model.

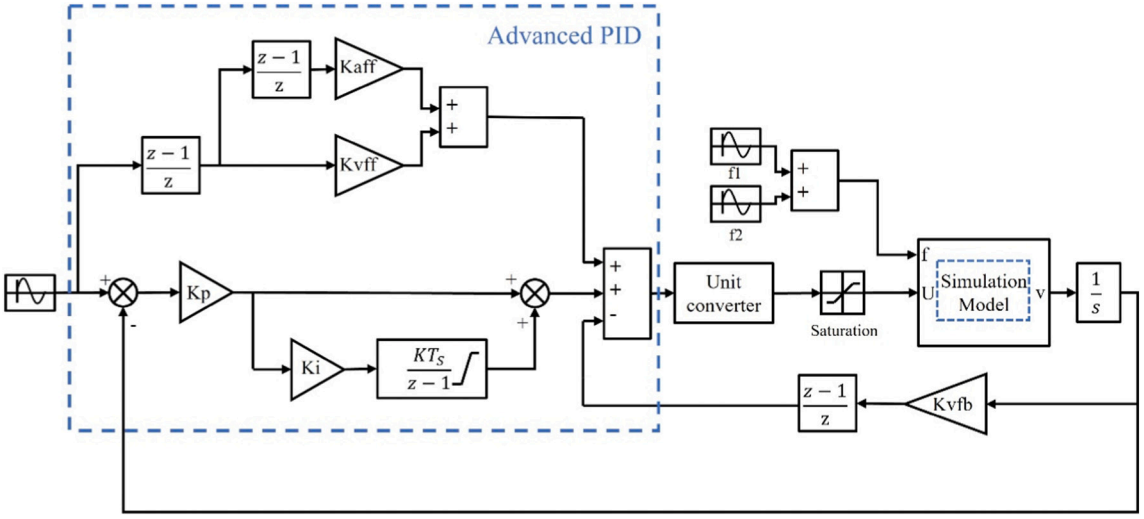

Fig. 7. Simulation of robustness test for advanced PID control.

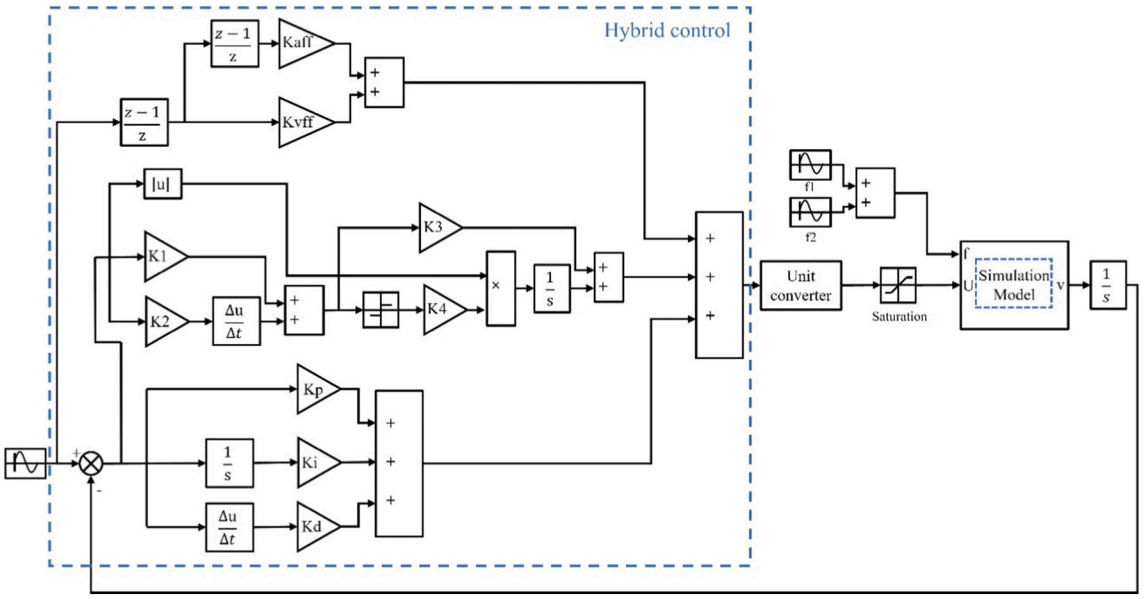

Fig. 8. Simulation of robustness test for hybrid control.

Table 2
Model parameters.

Advanced PID		Hybrid control		Other parameters	
K_p	1.9165	K_p	5.813	F1	10
K_p	0.0012	K_i	0.0013	F2	1
K_{vfb}	83.1842	K_d	0.0056	f	30/40
K_{vff}	83.1842	$K1$	12		
K_{aff}	1500	$K2$	0.08		
		$K3$	0.2		
		$K4$	0.1		
		K_{aff}	1600		
		K_{vff}	0.5		

control diagrams for these two algorithms are shown in Figs. 7 and 8 respectively. In the simulation, the external disturbance consists of two different forces: f_1 shares the same frequency with the system's working frequency which represents the cutting force; f_2 has double the frequency of f_1, representing certain types of frequency doubling disturbance. The total disturbance can be described as in Eq. (8), and the simulation parameters are given in Table 2.

$$f_{disturbance} = f1 + f2 = F1sin(2\pi ft) + F2sin(4\pi ft) \quad (8)$$

The input signal is 1 mm at 30 Hz and 0.5 mm at 40 Hz, and the control case is the simulation without disturbance *f*. The hybrid control gives better tracking performance than advanced PID control, according to our previous work [20]. In this paper, tracking error and the differences of the tracking error are calculated to evaluate the robustness of these two control algorithms. Fig. 9 shows the simulation results of the robustness test when the input sinusoidal signal is 1 mm at 30 Hz. The disturbance leads to increases in tracking error and also causes the amplitude and phase errors to increase. The results are calculated in the form of percentages and are provided in Tables 3 and 4.

From the simulation results, the hybrid control algorithm gives better robustness than the advanced PID control algorithm. The tracking error difference for hybrid control is only one-third of that for advanced PID control. Similar conclusions can be drawn from the comparison of amplitude and phase error differences. It can be noted that, with unlike tracking and amplitude error, phase error decreases due to the disturbance. This is because the disturbance is a resistance force for the motor force and decreases the motor output force essentially. From the control perspective, the controller adjusts the voltage output according to the error between the actual value and the required value due to the closed-loop system design. The system cannot follow the controller output instantaneously, which leads to phase error. When the required motor force decreases, the system follows the controller's output without delay, but this leads to large amplitude error. Therefore, the phase error difference is very small whereas the amplitude error difference is significant.

Besides, the FTS is designed to operate at different amplitudes and frequencies. Before the machining experiments, it is essential to run some actual no-load tests to assess the system performance at different input signals. The tracking error comparison results are shown in Table 5, and the system with the hybrid control algorithm shows better tracking performances.

4. Machining experiments

4.1. Experimental set-up

Four machining tests were designed to assess the effects of different control algorithms on the machining process. The designed FTS system was installed on the Z axis of an ultra-precision turning machine (Nanotech 650FGv2). A single crystal diamond tool with a nose radius of 0.25 mm, tool rake angle of 0°, and clearance angle of 9° was used in the machining experiments. A 40 mm diameter copper workpiece is clamped onto the machine spindle through a vacuum chunk. The FTS generates the sinusoidal motion, and the spindle rotates during the entire machining process. The experimental set-up is shown in Fig. 10, and the cutting parameters are listed in Table 6. In addition, the zero position is set at −0.99 or − 0.49 mm from the workpiece surface. These settings allow the FTS system to achieve a long stroke of ±1 or ± 0.5 mm, but the depth of cut is maintained at 10 μm.

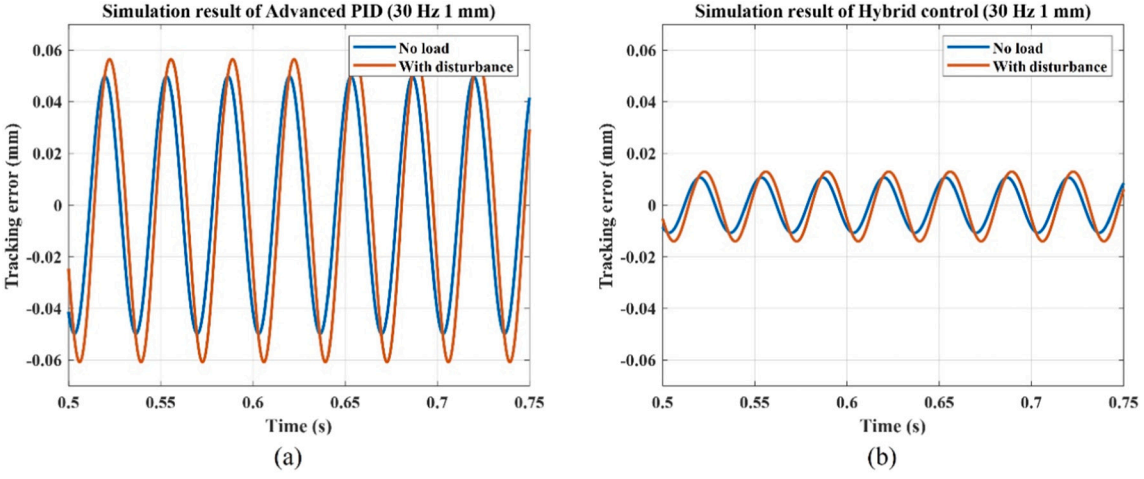

Fig. 9. Simulation results of robustness test: (a) advanced PID control; (b) hybrid control.

Table 3
Simulation results for tracking error (%).

	Stroke (mm)	Frequency (Hz)	No-load	Disturbance	Error difference
Hybrid control	1	30	1.067%	1.346%	0.279%
Advanced PID			4.984%	5.866%	0.882%
Hybrid control	0.5	40	1.294%	1.975%	0.681%
Advanced PID			6.106%	8.398%	2.292%

Table 4
Simulation results for amplitude and phase error (%).

	Amplitude error			Phase error		
	No-load	Disturbance	Difference	No-load	Disturbance	Difference
Hybrid (30 Hz)	0.641%	1.255%	0.614%	0.008%	0.008%	0.000%
Advanced PID (30 Hz)	2.671%	5.369%	2.698%	0.045%	0.033%	0.012%
Hybrid (40 Hz)	0.962%	2.038%	1.076%	0.009%	0.002%	0.007%
Advanced PID (40 Hz)	4.159%	8.749%	4.590%	0.037%	0.009%	0.028%

Table 5
Tracking error comparison results (%).

Tracking error (%)					
Input signal	1 mm 30 Hz	0.68 mm 40 Hz	0.43 mm 50 Hz	0.3 mm 60 Hz	0.1 mm 100 Hz
Advanced PID	1.211%	1.938%	3.135%	5.560%	15.576%
Hybrid control	0.364%	0.594%	0.871%	1.335%	3.740%

Apart from these four machining experiments, four corresponding no-load tests were also conducted as controls. These no-load tests shared the same FTS working parameters as in tests A-D, but the cutting tool did not touch the workpiece. The FTS motion profile during the machining experiments and no-load tests were recorded from the FTS encoder.

4.2. System motion profile

As in the simulation comparisons, the system tracking error can be calculated in terms of the difference between the actual and specified system motion profiles. Accuracy in the calculation of the phase error is problematic due to the difficulty of fully overlapping the starting points of the machining and no-load test results. However, the tracking error can be considered to be a combination of amplitude and phase errors. Therefore, the system motion profile comparisons use tracking error as the parameter. The tracking errors of tests A-D and the corresponding no-load tests are shown in Fig. 11.

Firstly, as expected, the disturbance (cutting force) in the machining experiments affects the system motion profile. Values of tracking error in all four tests have increased no matter which control algorithm is adopted. Secondly, the tracking error becomes non-sinusoidal and irregular due to the disturbance. Irregularities in tracking error means that the tool motion is not an ideally sinusoidal motion, which affects the final machining quality. The final surface quality can be tested during the subsequent examination of the microstructured surface. Finally, the tracking error and its increases are summarised in Table 7. As with the simulation results, the system with hybrid control exhibits better tracking performance (0.651% and 0.359%) than the system with advanced PID control (1.859% and 2.19%). Also, robustness has been demonstrated according to the increases in tracking error. The system with hybrid control exhibits increases in error of only 0.397% (test A) or 0.160% (test C), while the system with advanced PID control shows increases in error of 1.390% (test B) or 1.584% (test D).

Moreover, the first few periods of system motion show that the hybrid algorithm can offer more prompt control than advanced PID algorithm. The enlarged motion profile of the first few periods in Tests A

Table 6
Cutting parameters used in machining experiments.

Test	FTS stroke (mm)	FTS frequency (Hz)	Spindle speed (rpm)	Depth of cut (μm)	Feedrate (mm/min)	Control algorithm
A	±1	30	187	10	3	Hybrid
B	±1	30	187	10	3	Advanced PID
C	±0.5	40	253	10	3	Hybrid
D	±0.5	40	253	10	3	Advanced PID

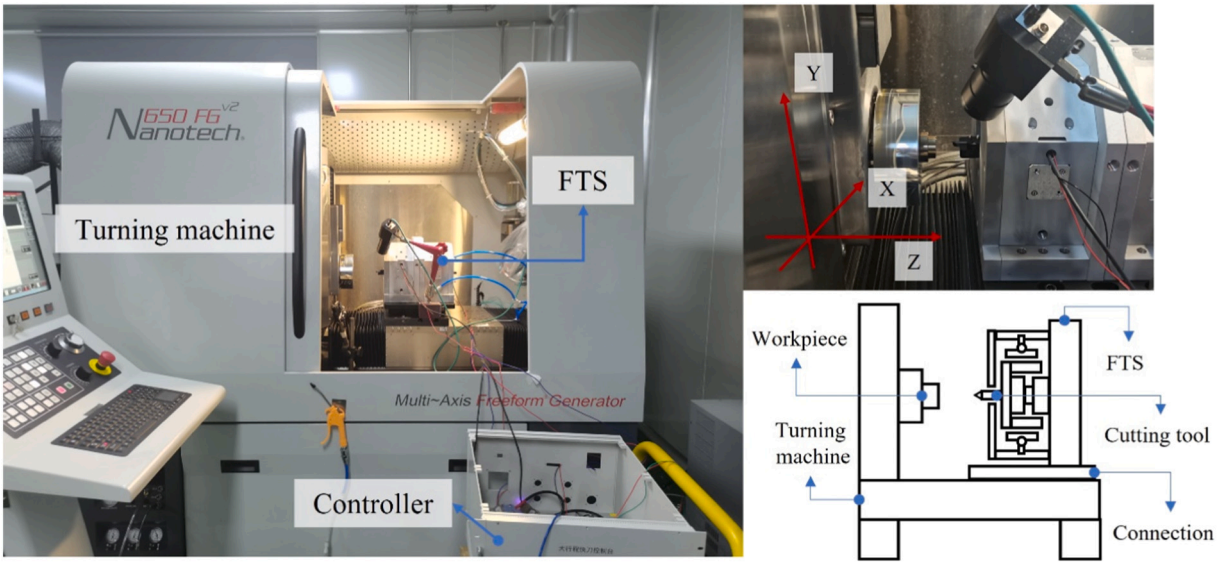

Fig. 10. Machining experiment set-up.

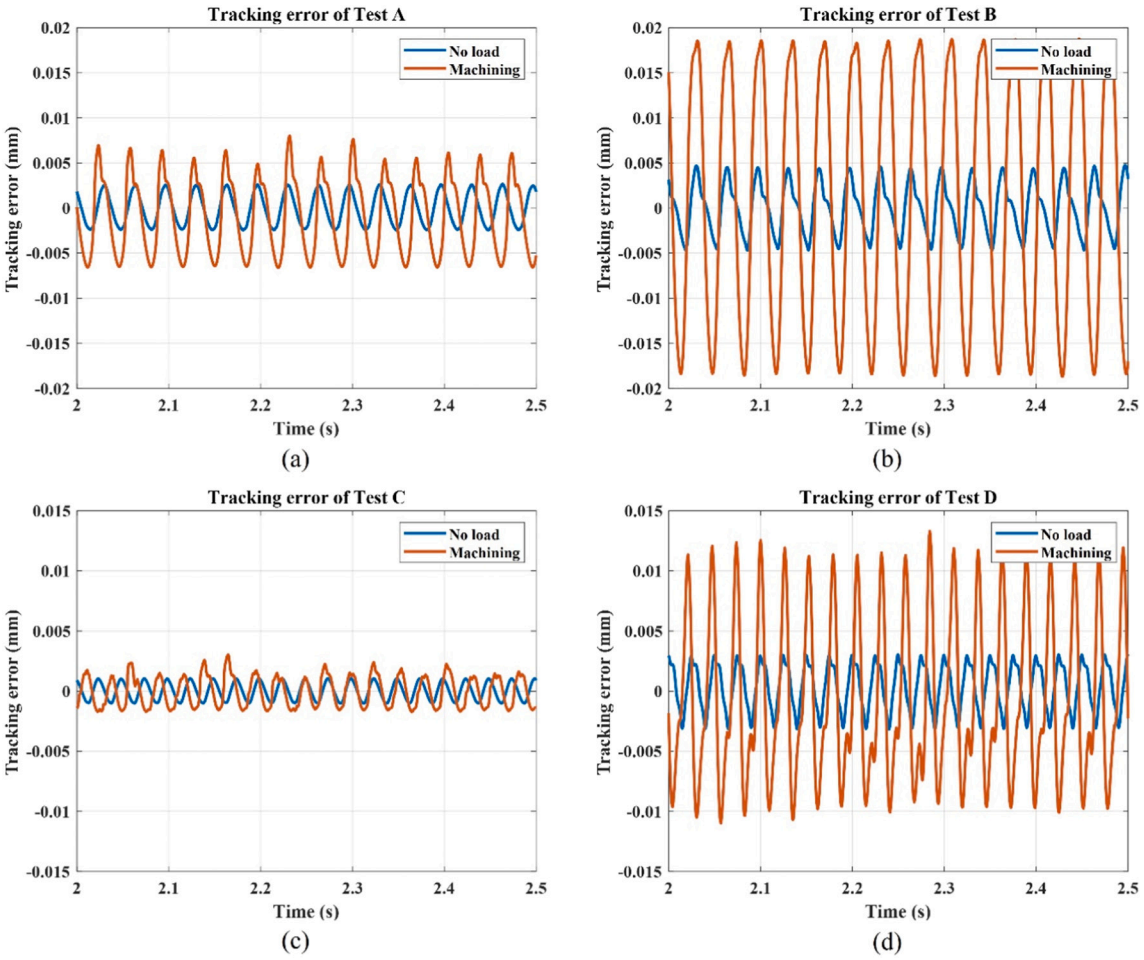

Fig. 11. FTS system tracking errors: (a) test A; (b) test B; (c) test C; (d) test D.

Table 7
Tracking error comparisons.

Test	No-load (mm)	%	Machining (mm)	%	Error increase
A	0.00254	0.254%	0.00651	0.651%	0.397%
B	0.00470	0.470%	0.01859	1.859%	1.390%
C	0.00099	0.198%	0.00179	0.359%	0.160%
D	0.00298	0.595%	0.01089	2.179%	1.584%

and B are shown in Fig. 12 (a) and (b) respectively. The FTS system in Test A reaches the target position after the first period. In Test B, the system reaches steady state only in the fourth period. The same results can be observed from Tests C and D. From the comparisons, the hybrid control algorithm offers a faster response than the advanced PID control algorithm. However, it is possible to increase the proportion parameter to speed up the system's response with advanced PID control. But, since the system is underdamped, an increase in the proportion parameter will

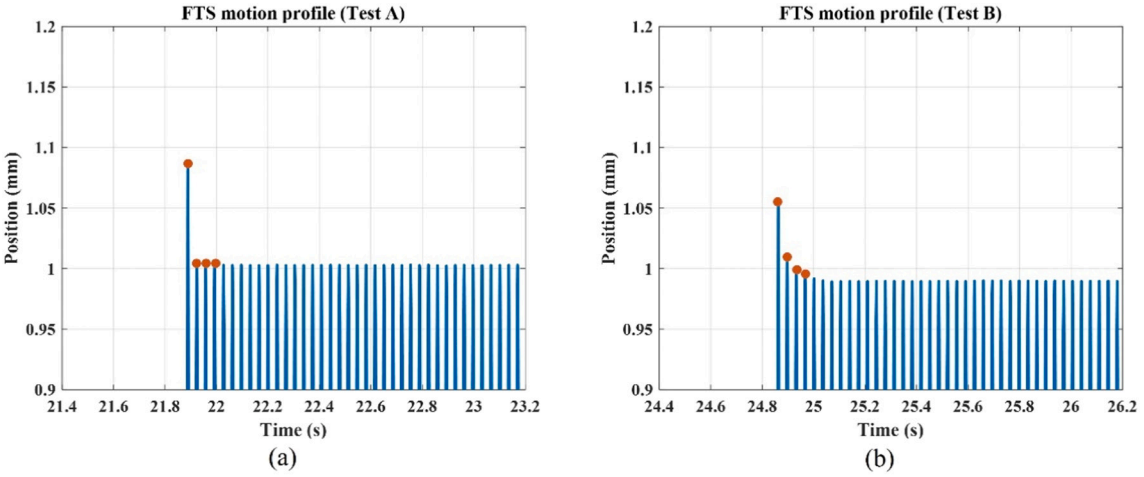

Fig. 12. Enlarged motion profile view: (a) test A; (b) test B.

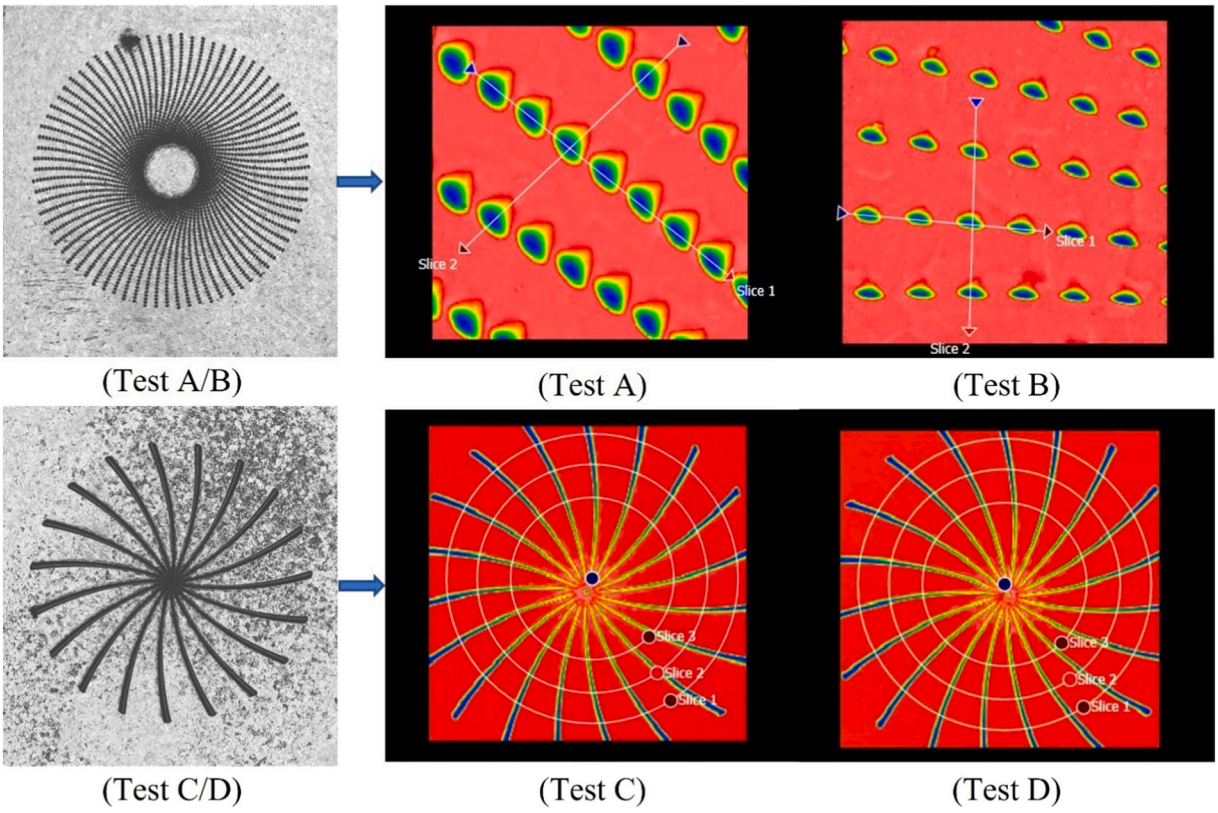

Fig. 13. Microstructed surface profile measurement using Zygo 3D surface profiler.

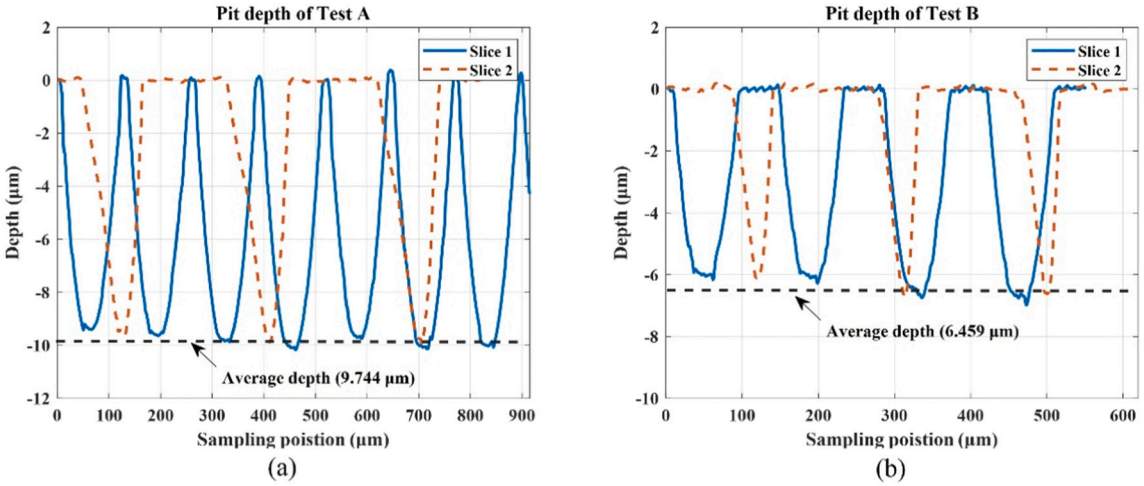

Fig. 14. Cutting depth: (a) test A; (b) test B.

be likely to result in an increase in overshoot, and a large overshoot may lead to system failure.

4.3. Microstructured surface profile

The robustness of the control algorithm is also reflected in the machined microstructured surface. A 3D optical surface profiler (Zygo Newview 9000) was adopted to measure the surface profile and roughness. The depth of the microstructured surface for tests A and B refers to the depth of discontinuous pits, while for tests C and D, it refers to the depth of the groove. Note that 19 grooves can be observed from tests C and D, and their depth is given as the average of all sampled grooves. Likewise, for tests A and B, the depth of the pits given is the average value of the sampled pits. The profile tests results are shown in Fig. 13.

Tests A and B share the same cutting parameters, as do tests C and D. The only difference is the control algorithm adopted. Therefore, the appearance of the machined surfaces remains similar. The slices in Fig. 13 are the sample slices, and the depth information can be drawn along the slices. The depths of pits and grooves are shown in Figs. 14 and 15, where only slice 2 in each of tests C and D are shown for simplification. The average depth information is provided in Table 8.

Referring to tests A and B, a more accurate depth profile is achieved with the help of the hybrid control algorithm. The cutting tool has not reached the target position in test B, since the original position of cutting tool has changed. The cutting depth error of 35.410% shows that the FTS

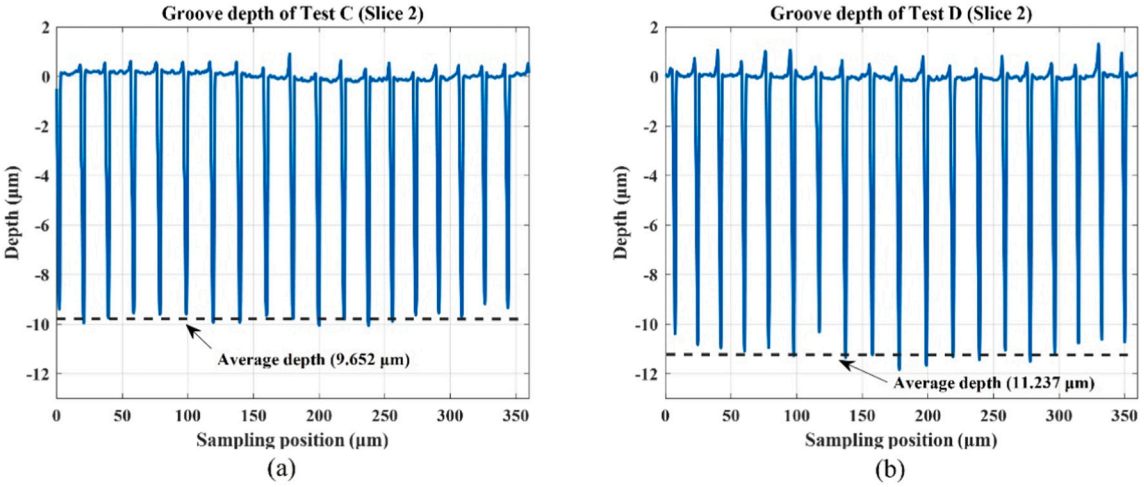

Fig. 15. Pit and groove depth: (a) test C; (b) test D.

Table 8
Depth and error.

Tests	Target depth (μm)	Average depth (μm)	Error
A	10	9.744	2.560%
B	10	6.459	35.410%
C	10	9.652	3.480%
D	10	11.237	12.370%

system with the advanced PID control algorithm exhibits weaker stiffness in the direction of motion, and therefore the system is more prone to be affected by disturbance than the system with hybrid control (2.560% error). A similar conclusion can be drawn from tests C and D. The results for test D demonstrate the overcutting problem and the depth error of 12.370% is much greater than the 3.480% depth error in Test C.

Surface roughness was also measured using the 3D surface profiler. A part of each machined surface was taken as the sampling area. For tests A and B, the sampling area is the surface at the bottom of the pits. For tests C and D, the central part of the groove is used as the sampling area. The surface roughness results and the sampling areas in tests A and C are shown in Fig. 16. Arithmetical mean height (Sa) is used to represent surface roughness. For tests A-D, the values of surface roughness measured are 0.368 μm, 0.328 μm, 0.236 μm and 0.321 μm respectively. The results show that surface roughness is not significantly affected by

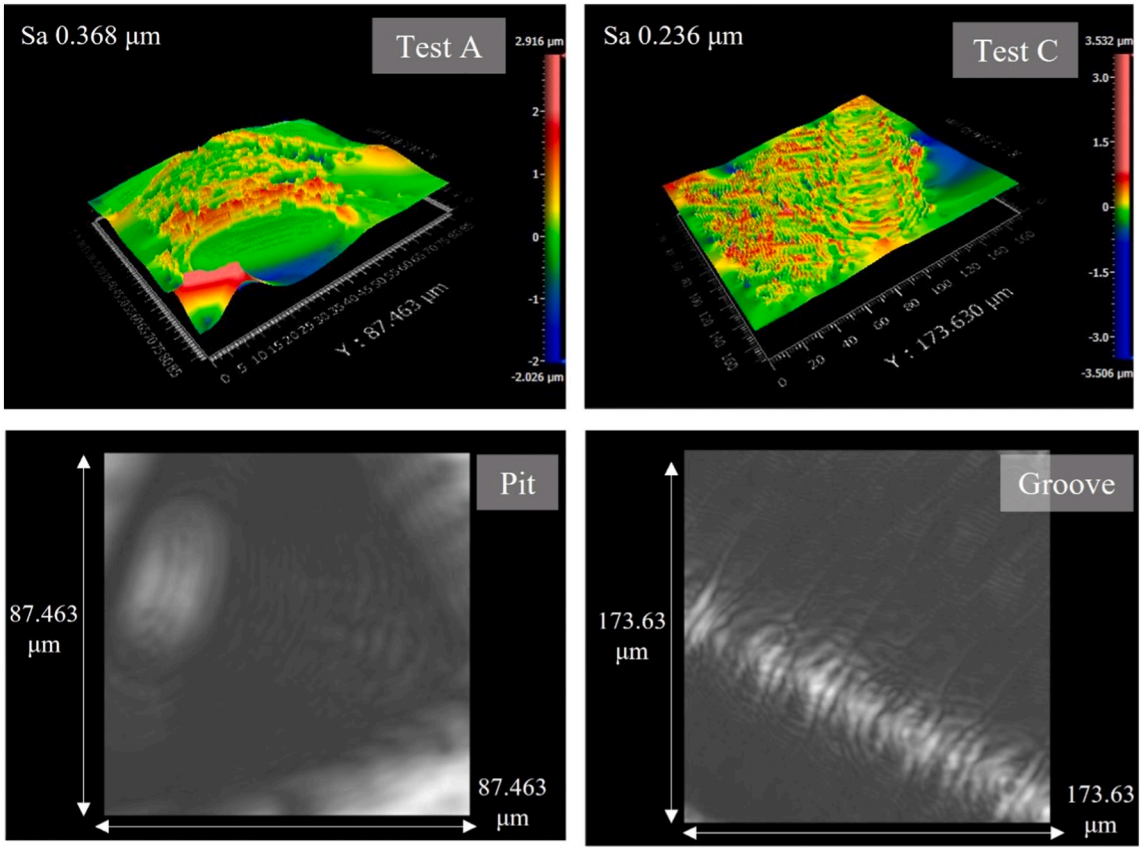

Fig. 16. Surface roughness measurement on the machined surfaces from tests A and C.

the control algorithm.

It should be noted that the values of cutting depth error and surface roughness obtained in these experiments are higher than those in the ultra-precision turning process where sub-micron form accuracy and nanometre-level surface roughness are typically achieved. This is because only rough machining tests were carried out, and the robustness of the control algorithms is more prominent during large feeds in rough machining.

Overall, control algorithm robustness can be reflected by the surface profile. The hybrid control algorithm helps the FTS to achieve higher surface profile accuracy and minimise overcut or undercut. On the other hand, the workpieces machined by the system with advanced PID control show significant surface profile errors with either overcut or undercut. Hybrid control shows better robustness than advanced PID control, which verifies the conclusions drawn from the system simulations and the effectiveness of the simulation model (Fig. 4). Therefore, the model can be used for further control algorithm development and predictions of system performance with different system parameters with different types of disturbance.

5. Conclusions

In this paper, the robustness of the advanced PID control and hybrid control algorithms are tested and compared on a designed LF-FTS system. The simulation model has been developed and verified by the machining experiments. The following conclusions can be drawn:

1. A mathematical simulation model was built and verified by the system identification model. When force disturbance was added to the simulation model, smaller error differences were observed for the system with the hybrid control algorithm compared with those observed with the advanced PID control. A similar conclusion can be drawn from the differences in amplitude error and phase error. This demonstrates the superior robustness of the hybrid control algorithm.
2. Four machining experiments were designed and conducted to evaluate the robustness of the control algorithms. From the system motion profiles, the increase in tracking error with the hybrid control algorithm was $<0.5\%$, while that using the advanced control was $>1\%$. Furthermore, the hybrid control algorithm provides a quicker response speed than the advanced PID control algorithm as shown by the transient responses of the system motion profiles.
3. Considering the quality of the microstructured surface, the hybrid control algorithm offers more accurate microstructural surface depth than advanced PID control. The cutting depth error decreased from 35.410% (12.370%) to 2.560% (3.480%). The hybrid control algorithm has better tracking performance than advanced PID control in the presence of disturbance.

Declaration of competing interest

The authors declare that they have no known competing financial interests or personal relationships that could have appeared to influence the work reported in this paper.

References

[1] Zhou L, Cheng K. Dynamic cutting process modelling and its impact on the generation of surface topography and texture in nano/micro cutting. ProcInstMechEngBJEngManuf Mar. 2009;223(3):247–66. https://doi.org/10.1243/09544054JEM1316.

[2] Li Z, Fang F, Chen J, Zhang X. Machining approach of freeform optics on infrared materials via ultra-precision turning. Opt Express 2017;25(3):2051. https://doi.org/10.1364/oe.25.002051.

[3] Sosnicki O, Pages A, Pacheco C, Maillard T. Servo piezo tool SPT400MML for the fast and precise machining of free forms. Int J Adv Manuf Technol 2010;47(9–12):903–10. https://doi.org/10.1007/s00170-009-2140-6.

[4] Zhu Z, Zhou X, Liu Q, Zhao S. Multi-objective optimum design of fast tool servo based on improved differential evolution algorithm. JMechSciTechnol 2011;25(12):3141–9. https://doi.org/10.1007/s12206-011-0824-y.

[5] Wang H, Yang S. Design and control of a fast tool servo used in noncircular piston turning process. MechSystSignal Process Mar. 2013;36(1):87–94. https://doi.org/10.1016/j.ymssp.2011.07.013.

[6] Tian F, Yin Z, Li S. A novel long range fast tool servo for diamond turning. Int J Adv Manuf Technol 2016;86(5–8):1227–34. https://doi.org/10.1007/s00170-015-8282-9.

[7] Feng H, et al. Fabrication of freeform progressive addition lenses using a self-developed long stroke fast tool servo. IntJAdvManufTechnol Aug. 2017;91(9–12):3799–806. https://doi.org/10.1007/s00170-017-0050-6.

[8] Liu Q, Zhou X, Liu Z, Lin C, Ma L. Long-stroke fast tool servo and a tool setting method for freeform optics fabrication. OptEng 2014;53(9):092005. https://doi.org/10.1117/1.oe.53.9.092005.

[9] Rakuff S, Cuttino JF. Development of a precision long-range fast tool servo system for diamond turning, vol. 3161850 [Online]. Available. The University of North Carolina at Charlotte; 2005. http://search.proquest.com/docview/305375292?accountid=14512%5Cnhttp://ucelinks.cdlib.org:8888/sfx_local?url_ver=Z39.88-2004&rft_val_fmt=info:ofi/fmt:kev:mtx:dissertation&genre=dissertations+&+theses&sid=ProQ:ProQuest+Dissertations+&+Theses+A&I&atitle=&ti.

[10] Lu X, Trumper DL. Electromagnetically driven fast tool servo. In: Proc. 18th Annual ASPE Meeting; 2003. p. 103–6.

[11] Lu X, Trumper DL. High bandwidth fast tool servo control. 2004. https://doi.org/10.23919/ACC.2004.1383692.

[12] Zhou X, Zhu Z, Zhao S, Luo D. A novel hybrid control strategy for trajectory tracking of fast tool servo. In: ICMEE 2010 - 2010 2nd International Conference on Mechanical and Electronics Engineering, Proceedings. vol. 2; 2010. V2-325–2-328. https://doi.org/10.1109/ICMEE.2010.5558416.

[13] Zhang H, Dong G, Zhou M, Song C, Huang Y, Du K. A new variable structure sliding mode control strategy for fts in diamond-cutting microstructured surfaces. Int J Adv Manuf Technol 2013;65(5–8):1177–84. https://doi.org/10.1007/s00170-012-4249-2.

[14] Duan F, le Zhu W, Sun A, Ju BF. Systematic modeling and rapid control for diamond machining of periodical optical surface. JManufProcess 2020;56(November 2019):451–62. https://doi.org/10.1016/j.jmapro.2020.05.003.

[15] Wu D, Chen K, Wang X. Tracking control and active disturbance rejection with application to noncircular machining. Int J Mach Tool Manuf 2007;47(15):2207–17. https://doi.org/10.1016/j.ijmachtools.2007.07.002.

[16] Lin CY, Chen PY. Precision tracking control of a biaxial piezo stage using repetitive control and double-feedforward compensation. Mechatronics 2011;21(1):239–49. https://doi.org/10.1016/j.mechatronics.2010.11.002.

[17] Buescher N, Dow T, Sohn A, Roblee J, Norland B. Live-axis turning. In: Proceedings of the 20th Annual ASPE Meeting,ASPE2005; 2005.

[18] Ku SS, Larsen G, Cetinkunt S. Fast tool servo control for ultra-precision machining at extremely low feed rates. Mechatronics 1998;8(4):381–93. https://doi.org/10.1016/s0957-4158(97)00063-9.

[19] Xie D, Zhu JQ, Wang F. Fuzzy PID control to feed servo system of CNC machine tool. Procedia Eng 2012;29:2853–8. https://doi.org/10.1016/j.proeng.2012.01.403.

[20] Gong Z, Huo D, Niu Z, Chen W, Shyha I. Investigation of control algorithm for long-stroke fast tool servo system. Precis Eng May 2022;75:12–23. https://doi.org/10.1016/j.precisioneng.2022.01.006.